Contents lists available at ScienceDirect

Applied Catalysis B: Environmental

Fabrication of TiO$_2$ nano-branched arrays/Cu$_2$S composite structure and its photoelectric performance

Keying Guo [a], Zhifeng Liu [a,*], Cailou Zhou [a], Jianhua Han [a], Yufeng Zhao [b,**], Zhichao Liu [a], Yajun Li [a], Ting Cui [a], Bo Wang [a], Jing Zhang [a]

[a] School of Materials Science and Engineering, Tianjin Chengjian University, 300384 Tianjin, China
[b] Department of Environmental and Chemical Engineering, Yanshan University, 066004 Qinhuangdao, China

ARTICLE INFO

ABSTRACT

Hierarchical nanostructured TiO$_2$ is known to be ideal materials for photoelectrochemical water splitting because of its excellent light harvesting efficiency, efficient charge separation and transport properties. In the present work, rutile TiO$_2$ nano-branched arrays (NBs) were grown directly on transparent conductive glass (FTO) using a simple two-step hydrothermal method. TiO$_2$ NBs/Cu$_2$S composite structure was subsequently synthesized through successive ionic layer adsorption and reaction (SILAR). Detailed growth mechanisms for TiO$_2$ NBs nanostructure and TiO$_2$ NBs/Cu$_2$S composite structure were discussed. The optical property of composite structures was characterized, and enhanced absorption spectrum was discovered. A much higher hydrogen generation efficiency of 13.15% at 0.70 V versus Ag/AgCl electrode was achieved for this TiO$_2$ NBs/Cu$_2$S composite structure. This is attributed to the improved light absorption and appropriate energy gap structure, which is over 40% higher than that of TiO$_2$ NWs/Cu$_2$S composite structure.

1. Introduction

As a potential source of clean and renewable energy, hydrogen energy has been considered as one of the benign candidates for traditional fossil energy since Fujishima and Honda reported the photoelectrochemical (PEC) production of hydrogen from water using TiO$_2$ electrodes in 1972 [1]. Hydrogen can be produced by a number of methods, such as photoelectrochemical (PEC) water splitting [2], thermochemical cycles [3], catalytic reforming of hydrocarbon fuels [4] and many others. Among them, PEC water splitting method has attracted significant attention in these years, because it is an environmentally friendly process without carbon dioxide emission. Meanwhile, numerous active photocatalysts have been applied as photoelectrode for PEC cells including TiO$_2$ [5–7], WO$_3$ [8], Fe$_2$O$_3$ [9], ZnO [10] and composited semiconductors [11,12]. Of all these photocatalysts, TiO$_2$ is currently one of the most extensively used due to its superior properties: high resistance to photocorrosion, low cost, good chemical stabilities, non-toxicity, superior charge transport properties and high photocatalytic activities [13–16].

However, bare TiO$_2$ still provides low hydrogen production efficiency, mainly due to the following reasons: (1) rapid recombination of photogenerated conduction band (CB) electrons and valence band (VB) holes on a bare TiO$_2$, (2) fast backward reaction between hydrogen and oxygen. Considerable attention has been drawn into the fabrication of TiO$_2$ with controlled nanostructures, including nanoparticles [17], nanowires (NWs) [18,19], nanorods (NRs) [19] and nanotubes (NTs) [20,21]. Nevertheless, the electron diffusion coefficient of these nanoparticulate films is several orders of magnitude smaller than the value in one-dimensional TiO$_2$ nanostructures, presumably due to electron traps at the contacts between nanoparticles [18]. Inspiringly, single-crystalline TiO$_2$ nanowires and nanorod arrays have been successfully prepared on FTO by hydrothermal method by Aydil in 2009 [19]. Wang et al. have recently synthesized rutile TiO$_2$ nano-branched arrays (NBs) grown directly on FTO by two-step wet chemical synthesis process in 2011 [22]. Cho and Chen et al. synthesized three kinds of nanostructured TiO$_2$ films made of nanoparticles, nanorods and branched nanorods (B-NRs), and the maximum applied bias photonto-current efficiency (ABPE) they got was 0.49% from B-NRs [13].

On the other hand, the spectrum of TiO$_2$ photoelectrodes can absorb is limited to UV region. Thus, many efforts have been put to increase the optical absorption of TiO$_2$, such as varying the chemical composition with metal (such as V [23]) or non-metal (such

* Corresponding author. Tel.: +86 2223085236; fax: +86 2223085110.
** Corresponding author. Tel.: +86 3358061569; fax: +86 3358061569.
E-mail addresses: tjulzf@163.com (Z. Liu), yufengzhao@ysu.edu.cn (Y. Zhao).

as N [24] and C [25]) doping, the deposition of narrow bandgap semiconductors (such as CdS [26], CdSe [27] CuInS$_2$ [28]). TiO$_2$ incorporated with sulfide semiconductors has been proven to be very effective ways to narrow its band gap energy and to enhance its hydrogen production efficiency. Li et al. have synthesized CdS nanocrystals by a hydrothermal method, and achieved the apparent quantum yield amounts to 13.9%, which is the highest activity for hydrogen production under visible light irradiation [29]. With CdSe nanostructures grown on the surface of TiO$_2$, Robel et al. were able to achieve 12% photon-to-charge carrier generation efficiency at full solar intensity [27]. Although CdS and CdSe have demonstrated high activity in hydrogen involved reactions in heterogeneous catalysis, both of them are toxic and sources limited. However, Cu$_2$S, a non-toxic and inexpensive catalyst has never been used as co-catalysts in PEC water splitting. Besides, Cu$_2$S is well known for its narrow band gap (1.1 eV) as a p-type semiconductor material [30]. It is widely used in photosensitizer of various wide band-gap semiconductor photoanodes [31,32], electronic and optoelectronic chips [33–35], etc.

To the best of our best knowledge, the synthesis of Cu$_2$S incorporated with TiO$_2$ NBs nanostructures for efficient PEC water splitting devices has never been investigated. Hence, in order to utilize more abundant solar light by increasing light scattering and absorption, we first prepared high densities of rutile TiO$_2$ NBs with enhanced surface-to-volume ratios on FTO via a facile two-step hydrothermal method. Secondly, different thicknesses of Cu$_2$S film were deposited on the surface of TiO$_2$ NBs by SILAR (successive ionic layer absorption and reaction) process. To illustrate the effect of the nanostructure, two kinds of PEC electrodes, TiO$_2$ NWs/Cu$_2$S PEC electrode and TiO$_2$ NBs/Cu$_2$S PEC electrode were designed and synthesized. Compared with the earlier studies, a much higher hydrogen generation efficiency of 13.15% for TiO$_2$ NBs/Cu$_2$S PEC electrode versus Ag/AgCl electrode was achieved, indicating a potential application for PEC water splitting. In addition, the synthetic process and working mechanism of the nanostructure were discussed.

2. Experimental

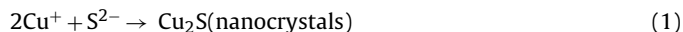### 2.1. The synthesis of high densities of TiO$_2$ NBs

In a typical synthesis process, 7 mL of deionized water and 0.50 mL ethylene glycol (EG) were mixed with 7.50 mL of concentrated hydrochloric acid (36.50–38% by weight). The mixture was stirred under ambient conditions for 5 min, and 0.16 mL of titanium butoxide was added to the mixture. Hydrochloric acid was used to avoid hydrolysis of the precursor by ensuring an acidic solution pH. After stirring for another 5 min, the mixture was placed in a Teflon-lined stainless steel autoclave of 20 mL volume. One piece of FTO substrate (F: SnO$_2$, 10 Ω square^{-1}), ultrasonically cleaned for 60 min in a mixed solution of deionized water, acetone and 2-propanol (volume rations of 1: 1: 1), was placed at an angle against the wall of the Teflon-liner with the conducting side facing down. Then, the sealed autoclave was put in an electric oven at 150 °C for 6 h. After cooling down to room temperature, the FTO substrate was taken out, washed with deionized water and ethanol several times, and dried in ambient air.

After the first-step hydrothermal reaction, TiO$_2$ nanoparticles were deposited on the TiO$_2$ NWs/FTO substrate as a seed layer by a dip-coating method using 0.20 M TiO$_2$ sol. The seed layer was obtained after annealing in air at 450 °C for 1 h. Another hydrothermal process was subsequently carried out to elongate the sprouts for the formation of branches on the TiO$_2$ NWs. Briefly, the branches are grown on the surface of the TiO$_2$ NWs using hydrothermal method by immersing the seeded-TiO$_2$ NWs in a sealed

autoclave filled with an aqueous solution of 12 mL ethanol, 0.10 mL of concentrated hydrochloric acid (36.50–38.00% by weight), and 0.20 mL titanium butoxide. The autoclave was sealed and kept at a constant temperature of 150 °C for 1.5 h. The TiO$_2$ NBs on FTO were finally obtained and rinsed with ethanol and dried in air at 100 °C.

2.2. Synthesis of TiO$_2$ NBs/Cu$_2$S composite structure

TiO$_2$ NBs/Cu$_2$S composite structure was synthesized by SILAR method. The saturated CuCl aqueous solution and 5 mM Na$_2$S at 25 °C were used in the deposition of Cu$_2$S nanoparticles on TiO$_2$ NBs to obtain the photoelectrochemical (PEC) electrodes. During the preparation of TiO$_2$ NBs/Cu$_2$S composite structure, the TiO$_2$ NBs sample was firstly immersed in the cationic precursor solution for 60 s, causing Cu$^+$ to be adsorbed on the surface of TiO$_2$ NBs. Secondly, this sample was immersed in an ample amount of deionized water for 60 s to prevent homogenous precipitation. Thirdly, the sample was then immersed in the anionic precursor solution for 60 s. S^{2-} reacted with the adsorbed Cu$^+$ on the surface of nano-branched arrays. Finally, the sample was then immersed in deionized water for 60 s. Thus, one cycle of Cu$_2$S deposition on the surface of TiO$_2$ NBs completed. The incorporated amount of Cu$_2$S can be increased by repeating the assembly cycles. The following chemical reactions could take place during the SILAR cycle:

$$2Cu^+ + S^{2-} \rightarrow Cu_2S(\text{nanocrystals}) \tag{1}$$

2.3. Characterization of samples

The morphologies of the samples were studied using a PHILIPS XL-30 scanning electron microscope (SEM) and HITACHI H-7650 transmission electron microscopy (TEM) operated at an accelerating voltage of 100 kV. The EDS spectra on the samples were also obtained with a PHILIPS XL-30 scanning electron microscope (SEM). The X-ray diffraction (XRD) analysis of the nanowire array was performed using a Rigaku D/max-2500 using Cu Kα radiation (λ = 0.154059 nm). Optical absorbance of photoanodes films was examined by DU-8B UV–vis double-beam spectrophotometer. Photoelectrochemical characterization of the samples was performed using an electrochemical workstation (LK2005A, Tianjin, China), a three-electrode configuration, with TiO$_2$ nanostructures on FTO-glass as the working photoelectrode, saturated Ag/AgCl as reference electrode, and a platinum foil as counter electrode. The potential was swept linearly at a scan rate of 50 mV s^{-1}. PEC water splitting experiments were conducted in NaOH electrolyte (1 mol/L). The working electrode was illuminated with a xenon lamp (CHF-XM500, 100 mW cm^{-2}). The stability of TiO$_2$ NBs/Cu$_2$S composite structure was measured by current–voltage (C–V) scanning from −0.60 to 0.80 V for 1 and 20 cycles under illumination (100 mW cm^{-2}).

3. Results and discussion

The synthetic route for TiO$_2$ NBs/Cu$_2$S composite structure is illustrated in Fig. 1. Oriented TiO$_2$ nanowire film could only be grown on FTO substrates successfully due to the fact that the FTO substrate also has the tetragonal rutile structure, and the lattice mismatch between the tetragonal FTO (a = b = 0.4687 nm) and rutile TiO$_2$ (a = b = 0.4593 nm) is 2% [19]. The small lattice mismatch between the FTO substrate and rutile TiO$_2$ plays a key role in driving the nucleation and growth of the rutile TiO$_2$ nanowires on FTO. A possible crystal growth mechanism of TiO$_2$ NWs on FTO substrate was proposed. It is reported that the different acid concentration leads to a different hydrolysis rate of tetrabutyl titanate, and forms the different amount of rutile TiO$_2$ crystal nucleus in the solution [17,18]. At the appropriate hydrochloric acid concentration of 6 M,
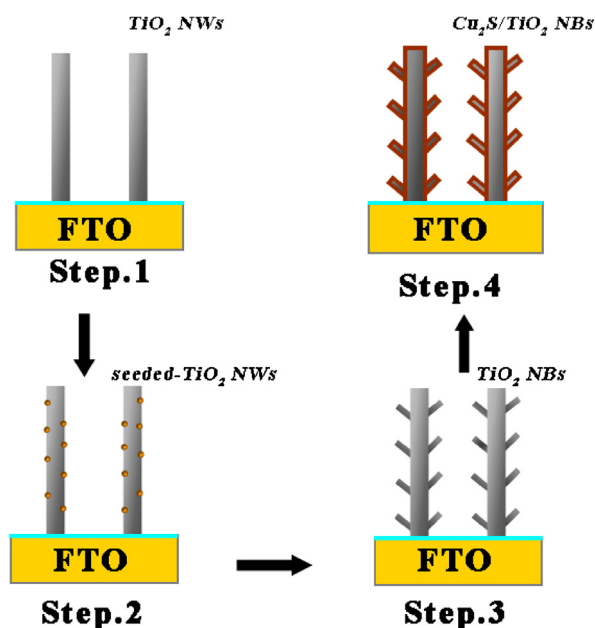
Fig. 1. Schematic illustration for the synthetic route of TiO$_2$ NBs/Cu$_2$S composite structure.

the tetrabutyl titanate dehydrates slowly, and the TiO$_2$ nucleus clusters are small and have crystal plane trends to some extent. EG also can retard the hydrolysis rate of titanium butoxide during the hydrothermal process and assists in nanoribbon growth as "cosurfactant" an "cosolvent" in an aqueous system [36]. With the reaction beginning, the amount of TiO$_2$ crystal nucleus and Ti^{4+} ions both increase gradually. The crystal growth is initiated preferentially from the most thermodynamically active clusters on the surface of the multimers, due to a supersaturated Ti^{4+} solution in their surroundings. And then TiO$_2$ nanowires begin to grow on the FTO substrate with the rod axis aligned approximately perpendicular to the FTO substrate. As a result, the multimers form ordered nanowires by assembly along the (1 1 0) direction by means of the Ostwald ripening process. Finally, the TiO$_2$ NWs/FTO was obtained as shown in Step 1. In Step 2, TiO$_2$ nanoparticles were deposited on the TiO$_2$ NWs/FTO substrate as a seed layer by a dip-coating method and the seeded-TiO$_2$ NWs were obtained after annealing in air. As shown in Step 3, the branches are grown on the surface of the TiO$_2$ NWs using hydrothermal method by immersing the seeded-TiO$_2$ NWs in a sealed autoclave filled with an aqueous

solution of ethanol, concentrated hydrochloric acid, and titanium butoxide. In Step 4, TiO$_2$ NBs/Cu$_2$S composite structure was synthesized by SILAR method. CuCl and Na$_2$S were used in the deposition of Cu$_2$S nanoparticles on TiO$_2$ NBs to obtain the PEC electrodes. During the preparation of TiO$_2$ NBs/Cu$_2$S composite structures, the TiO$_2$ NBs samples were immersed in the cationic precursor solution, deionized water, anionic precursor solution and deionized water in turn.

Fig. 2 shows the SEM images and XRD pattern of TiO$_2$ NWs grown on the FTO substrate by hydrothermal synthesis method using an aqueous solution of HCl and titanium butoxide at 150 °C for 6 h. It can be seen from Fig. 2A and B, well-aligned TiO$_2$ NWs have been fabricated on the FTO glass substrate after the hydrothermal growth. Fig. 2A is a low magnification image of the bare TiO$_2$ NWs, which reveals that the entire surface of the FTO substrate is covered very uniformly with TiO$_2$ NWs. Fig. 2B is a high magnification SEM image of the arrays, which indicates that the surfaces of the NWs are smooth. From the enlarged view in the inset of Fig. 2B, it can be seen that the TiO$_2$ NWs present a diameter of approximately 60 nm. Fig. 2C displays the XRD patterns of the FTO substrate before and after the hydrothermal reaction. As we all know, the FTO glass (F: SnO$_2$) is an transparent conductive fluorine-doped tin oxide substrate. Fig. 2C(a) shows the XRD patterns of the pure FTO substrate. As shown in Fig. 2C(a), FTO substrates have a tetragonal rutile phase of SnO$_2$ (JCPDS file No. 41-1445). Fig. 2C(b) shows that TiO$_2$ NWs deposited on FTO substrates are rutile TiO$_2$. All the diffraction peaks that appear upon nanowire growth agree well with the tetragonal rutile phase (JCPDS file No. 21-1276), a significantly enhanced (0 0 2) peak at a 2-theta of 63.20° indicates that the nanowires are well crystallized throughout their length and grow preferentially along the [0 0 1] direction with the growth axis perpendicular to the substrate.

TiO$_2$ NBs nanostructures are derived from the NWs and Fig. 3A–C show the low and high magnification SEM images, respectively. After the first-step hydrothermal reaction, TiO$_2$ nanoparticles were deposited on the TiO$_2$ NWs/FTO substrate as a seed layer, followed by calcination at 450 °C for 1 h in air. The framework of the nanowire arrays still exists on the FTO substrates, and a mass of branches were further formed along backbones of the TiO$_2$ NWs after second-step hydrothermal growth in an aqueous solution of 12.00 mL ethanol, 0.10 mL of concentrated hydrochloric acid and 0.20 mL titanium butoxide for 1.5 h, as shown in Fig. 3A–C. Each TiO$_2$ nanowire is enclosed by nanobranches, which can greatly improve the specific surface area and roughness factor of the TiO$_2$ NWs. From the enlarged view in the inset of Fig. 3C, it can be seen that the TiO$_2$ NBs present a diameter of approximately 60 nm. XRD patterns of the bare TiO$_2$ NWs and the TiO$_2$ NBs are shown in Fig. 3D(a) and (b),
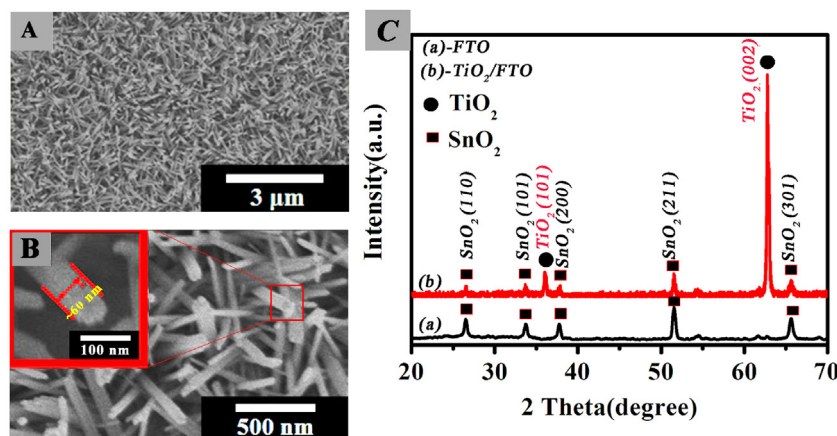

Fig. 2. Morphologies of TiO$_2$ NWs: typical top view SEM images of TiO$_2$ NWs at (A), and (B) high magnification; (C) XRD patterns of FTO (a) and TiO$_2$ NWs/FTO (b).
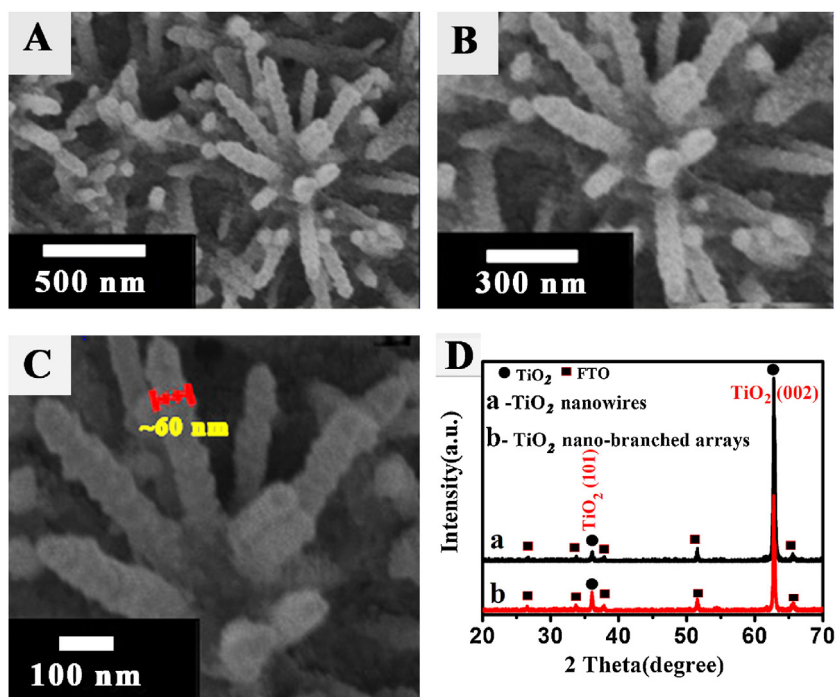
Fig. 3. Morphologies of TiO_2 NBs: typical top view SEM images of TiO_2 NBs at (A) low and (B) and (C) high magnifications; (D) XRD patterns of TiO_2 NBs.
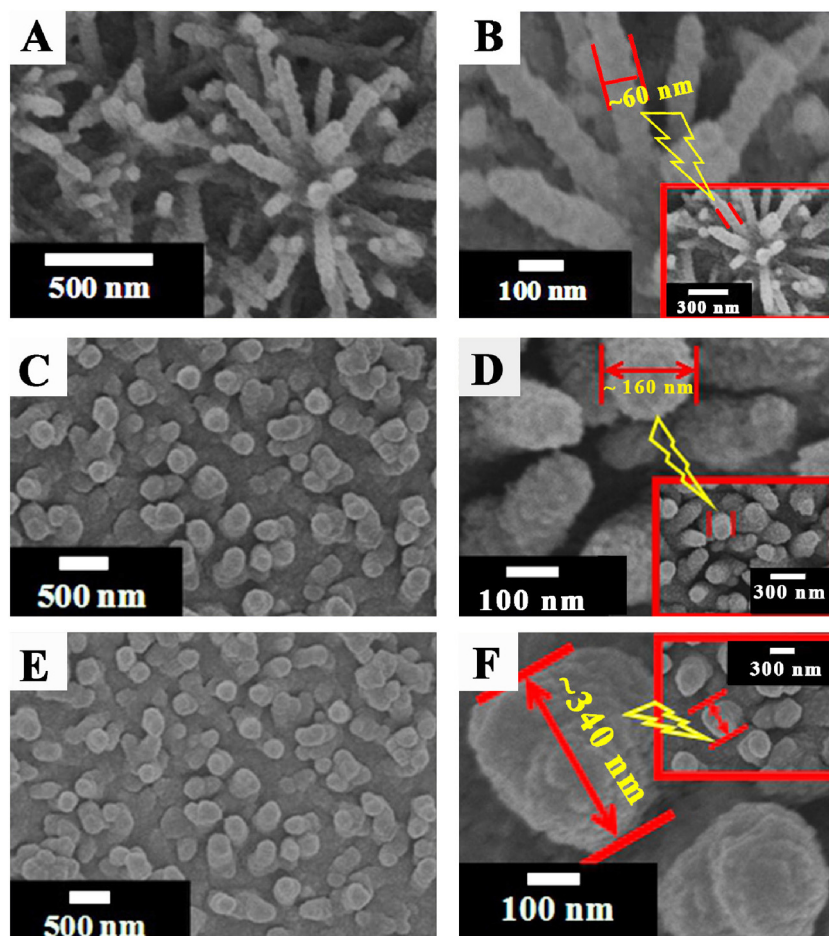

Fig. 4. Typical top view SEM images of TiO_2 NBs after branch growth reaction for different times: (A) and (B) 1.5 h; (C) and (D) 4 h; (E) and (F) 12 h.
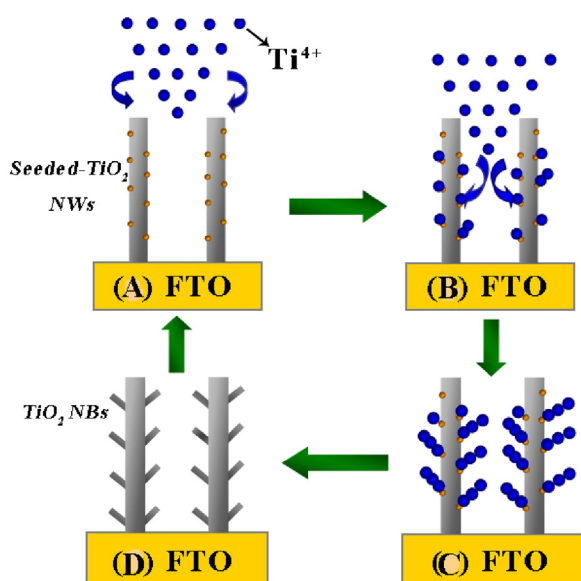
Fig. 5. Schematic representation of growth mechanism for TiO_2 NBs.

Fig. 6. Photograph of (A) pristine TiO_2 film and (B) TiO_2 NBs/Cu_2S film on FTO substrate.

respectively. Compared with the XRD patterns of TiO_2 NWs in curve a, curve b reveals that the TiO_2 NBs deposited on FTO substrates are also rutile TiO_2 and the peak intensity of the (0 0 2) becomes weak due to the fact that the oriented nanowire arrays are enclosed by non-oriented nanobranches of poor crystalline quality.

Fig. 4 presents the SEM images of TiO_2 NBs on FTO after branch growth reaction for different times in the second-step hydro-thermal progress and a possible crystal growth mechanism of rutile TiO_2 NBs is proposed, shown as in Fig. 5. Fig. 4A and B demonstrates that a mass of branches were successfully grown along backbones of the TiO_2 NWs. The diameter of the branches is about 60 nm after 1.5 h growth. After being immersed in the growth solution at 150 °C, the titanium butoxide hydrolysis precursor Ti^{4+} migrated into the seed layer, where nucleation occurred at high energy sites, and a large number of tiny TiO_2 crystallites began to germinate on the surfaces of the primary TiO_2 NWs. Simultaneously, Ti^{4+} precursors will hydrolyze with water at the water/TiO_2 NWs interface, result-ing in the formation of a crystal nucleus on the seed layer [36]. With continuous hydrolysis and subsequent growth-crystallization, the crystal nucleus grows fast due to high temperature and abun-dant Ti^{4+} in the solution. At the same time, the branch crystal nuclei are formed via the heteronucleation on the surface of the TiO_2 NWs, which grow into branches and made the surface of the nanowires become rougher, as shown in Fig. 5A–D. When the reaction time was longer than 1.5 h, the branched nanostructures
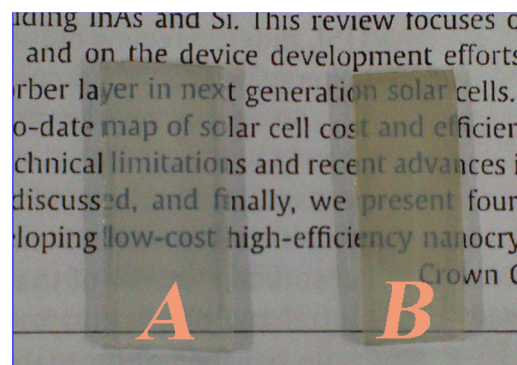
were not obtained. With the increasing growth period, the branches became nanorods and the diameter was nearly 160 nm, as shown in Fig. 4C and D. After the 12 h hydrolysis reaction, the nanorods became even larger and the diameter reached to nearly 340 nm, as shown in Fig. 4E and F.

After reactions in the solution with different condition, the color of the samples is darker than the bare one, indicating that Cu_2S was coated on the surface of TiO_2 NBs, shown as in Fig. 6.

Fig. 7 gives SEM images and the XRD pattern of the obtained TiO_2 NWs/Cu_2S composite structure of 10 cycles SILAR deposition. The top facets of the undecorated TiO_2 NWs appear to contain many step edges, while the surfaces of TiO_2 NWs are smooth. Once the Cu_2S nanoparticles modification was conducted on the surfaces of TiO_2 NWs, the top facets of the nanowires became flattened, the nanowires became adherent to each other, and the side facets demonstrated a rough appearance with vast quantities of minute particles inlaid, as shown in Fig. 7A. This latter observation indi-cates that the Cu_2S nanoparticles were indeed deposited onto the surfaces of the TiO_2 nanowires by SILAR method. In the XRD pattern of Fig. 7B, corresponding to the diffraction peaks of the TiO_2 NWs, the diffraction peaks with 2θ value around 26.5°, 37.4°, 54.6°, 61.4°, 68.9° could be observed, which can be indexed to the (0 0 2), (1 0 2), (0 0 4), (1 0 4), (2 0 3) plane of Cu_2S (JCPDS file No. 26-1116), respec-tively, indicating the formation of the TiO_2 NWs/Cu_2S composite structure by the SILAR process.

Fig. 8 illustrates the XRD pattern of the TiO_2 NBs/Cu_2S composite structure of 10 cycles SILAR deposition. The main diffractions peaks are identical to those of the Cu_2S (JCPDS file No. 26-1116), justifying the formation of the TiO_2 NBs/Cu_2S composite structure from SILAR deposition.

Fig. 9A–C shows top view images of a typical as-synthesized composite structure sample at low and high magnification,
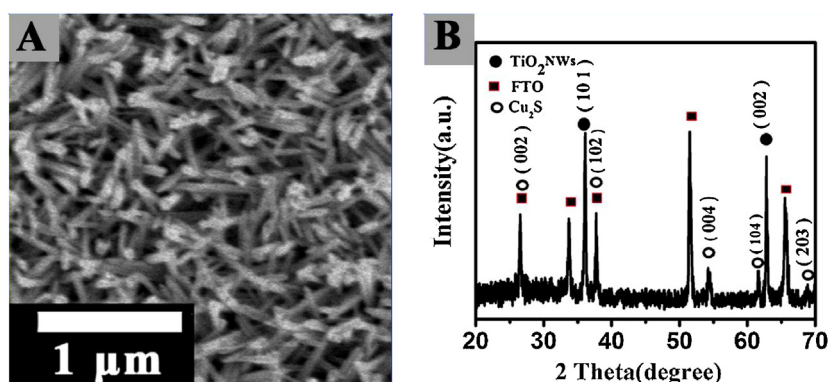

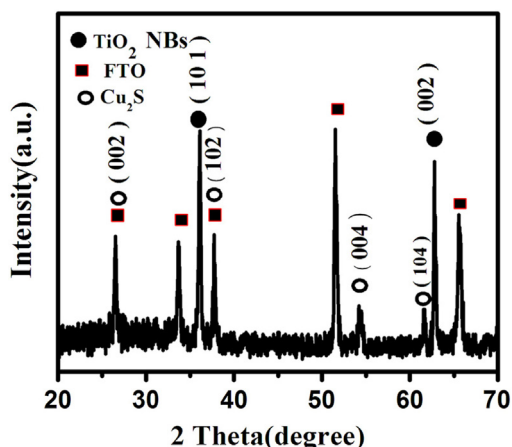**Fig. 7.** (A) SEM images of TiO_2 NWs/Cu_2S composite structure; (B) XRD pattern of TiO_2 NWs/Cu_2S composite structure.

Fig. 8. XRD patterns of TiO$_2$ NBs/Cu$_2$S composite structure of 10 cycles SILAR deposition.

Table 1
The photocurrent density and efficiencies of hydrogen generation of PEC electrodes.

PEC electrodes	Photocurrent density (mA cm^{-2})	Efficiencies of hydrogen generation (%)
TiO$_2$ NWs	5.05	6.00
TiO$_2$ NBs	8.63	9.30
TiO$_2$ NWs/Cu$_2$S composite structure of 10 cycles SILAR deposition	17.03	9.35
TiO$_2$ NBs/Cu$_2$S composite structure of 10 cycles SILAR deposition	24.85	13.15

respectively. As we can see in the SEM images, the obtained products inherit the morphology of pre-prepared TiO$_2$ NBs. Compared with a diameter of the same TiO$_2$ NBs sample, the TiO$_2$ NBs/Cu$_2$S composite structures obtained with 10 SILAR cycles present a diameter of approximately 85 nm, as shown in Fig. 9C. It is important to directly observe the Cu$_2$S nanoparticles on TiO$_2$ surface. The TEM can provide detailed microscopic information on the size of Cu$_2$S nanoparticles and their distribution over the TiO$_2$ NBs, which is crucial in understanding how they are deposited and how they would affect the photoelectrochemical properties of electrodes. Fig. 9D shows the TEM image of TiO$_2$ NBs deposited with Cu$_2$S for 10 SILAR cycles, displaying that the bare surface of TiO$_2$ NBs appears to be covered by a thin shell consisting of a large amount of smaller particles. So it can demonstrate that Cu$_2$S layer with a thickness of ~12 nm is almost uniform on top and side planes of the TiO$_2$ NBs. Furthermore, the corresponding size distribution in the yellow arrows of Fig. 9C indicates that Cu$_2$S nanoparticles with an average size of ~4 nm were deposited on the TiO$_2$ NBs surfaces.

The chemical stoichiometry of the TiO$_2$ NBs/Cu$_2$S composite structure was further examined with EDS, and the atomic ratio of S to Cu was found to be 1:2, as shown in Fig. 10.

Fig. 11 displays the room temperature absorbance spectra of TiO$_2$ NWs, TiO$_2$ NBs, TiO$_2$ NWs/Cu$_2$S composite structure, TiO$_2$ NBs/Cu$_2$S composite structure. The datum were recorded in the wavelength range of 300–900 nm and the absorption edges were approximately 400(A), 410(B), 470(C), 510(D) nm, respectively. It can be seen that the TiO$_2$ NBs/Cu$_2$S composite structure shows broader absorption region than that of the TiO$_2$ NWs/Cu$_2$S composite structure, mainly due to the reason that the former can make better use of the sunlight. First of all, light would be reflected

much more times among the branches and the multiple reflections would extend the light propagation path, which is beneficial to the full utilization of incident light. It can be seen that the TiO$_2$ NBs/Cu$_2$S composite structure shows a best absorbance in the visible region (centered at ~510 nm), indicating an enhancement in absorbing visible light. For the TiO$_2$ NBs/Cu$_2$S composite structure, a high efficiency of light-harvesting can be obtained by fabricating well-aligned NBs as photoelectrode. Cu$_2$S nanoparticles on the NBs surface can improve the light utilization efficiency by reflect unabsorbed photons back to NBs, which is beneficial to the full utilization of incident light. Meanwhile, increasing the photon absorption through the lager specific surface area of TiO$_2$ NBs, a layer of accumulated Cu$_2$S nanoparticles can trap relatively more photons, and thus larger amount of photons would be utilized by the TiO$_2$ NBs/Cu$_2$S composite structure for producing electron/hole pairs. What is more, vertical TiO$_2$ arrays grown on the FTO glass can directly transport the photo-induced electrons with a high speed, which take full advantages of the excellent carrier transport performance of as-obtained samples. Owing to the narrow band-gap of Cu$_2$S, the TiO$_2$ NWs/Cu$_2$S and the TiO$_2$ NBs/Cu$_2$S can absorb more visible light, which offers a broader range of absorption spectrum than pure TiO$_2$, shown as in Fig. 11C and D.

The PEC properties of various composite structures were characterized using a three-electrode PEC system, and Fig. 12 and Table 1 show the photocurrent density versus applied potential characteristics of the (A) TiO$_2$ NWs, (B) TiO$_2$ NBs, (C) TiO$_2$ NWs/Cu$_2$S composite structure of 10 cycles SILAR deposition, (D) TiO$_2$ NBs/Cu$_2$S composite structure of 10 cycles SILAR deposition, measured in NaOH electrolyte (1 mol/L) under Xe light illumination of 100 mW cm^{-2}. It can be seen that the photocurrent densities of (A) bare TiO$_2$ NWs, (B) TiO$_2$ NBs, (C) TiO$_2$ NWs/Cu$_2$S composite structure, (D) TiO$_2$ NBs/Cu$_2$S composite structure, were 5.05 mA cm^{-2} at −0.05 V versus Ag/AgCl, 8.63 mA cm^{-2} at −0.15 V versus Ag/AgCl, 17.03 mA cm^{-2} at 0.68 V versus Ag/AgCl, 24.85 mA cm^{-2} at 0.70 V versus Ag/AgCl, respectively. After coated with Cu$_2$S, TiO$_2$ NBs/Cu$_2$S composite structure showed much higher photocurrent density
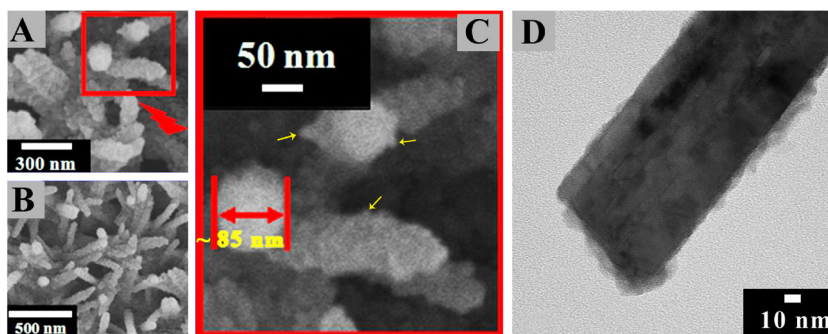

Fig. 9. Morphologies of TiO$_2$ NBs/Cu$_2$S composite structure of 10 cycles SILAR deposition: typical top view SEM images at (A), (B) low and (C) high magnifications; (D) TEM image of TiO$_2$ NBs/Cu$_2$S composite structure of 10 cycles SILAR deposition.
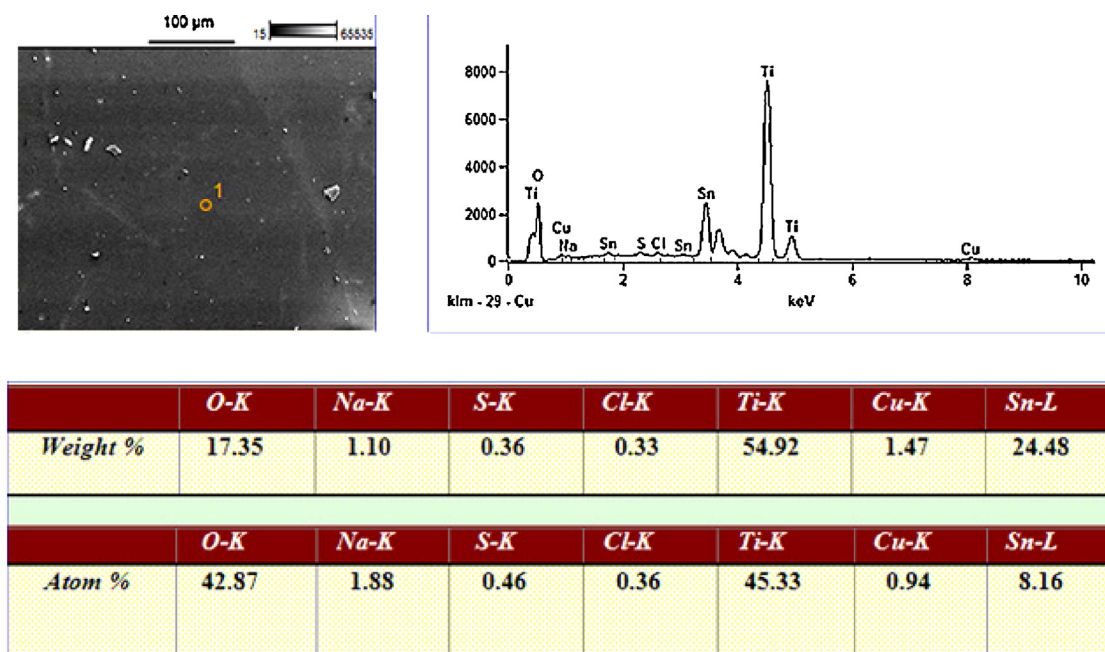
	O-K	Na-K	S-K	Cl-K	Ti-K	Cu-K	Sn-L
Weight %	17.35	1.10	0.36	0.33	54.92	1.47	24.48

	O-K	Na-K	S-K	Cl-K	Ti-K	Cu-K	Sn-L
Atom %	42.87	1.88	0.46	0.36	45.33	0.94	8.16

Fig. 10. EDS patterns of the TiO$_2$ NBs/Cu$_2$S composite structure of 10 cycles SILAR deposition.

24.85 mA cm^{-2} at 0.70 V versus Ag/AgCl than that of TiO$_2$ NWs/Cu$_2$S composite structure (17.03 mA cm^{-2} at 0.68 V versus Ag/AgCl). The highest photocurrent density, 24.85 mA cm^{-2} at 0.70 V versus Ag/AgCl, was obtained by using TiO$_2$ NBs/Cu$_2$S composite structure as electrode.

Based on the assumption that all of the photocurrent flowing from the photoelectrode to the Pt counter electrode was consumed for hydrogen generation, the efficiencies of hydrogen generation (η) could be calculated according to the following equation [10]:

$$\eta = \left[\frac{J_p(E^{\circ}_{rev} - |E_{app}|)}{I_{light}} \right] \times 100\% \qquad (2)$$

where J_p is the photocurrent density (mA cm^{-2}), E°_{rev} is the standard reversible potential which is 1.23 V, E_{app} is the applied external potential and I_{light} is the intensity of the solar simulated incident light, which was 100 mW cm^{-2} in this study. The hydrogen generation efficiency of various electrodes can be obtained based on the photocurrent density shown in Fig. 12 and Table 1. The maximum hydrogen generation efficiencies of 6.00%, 9.30%, 9.35%, 13.15% for

the TiO$_2$ NWs solar PEC electrode at −0.05 V bias, the TiO$_2$ NBs solar PEC electrode at −0.15 V bias, the TiO$_2$ NWs/Cu$_2$S composite structure solar PEC electrode at 0.68 V bias, the TiO$_2$ NBs/Cu$_2$S composite structure solar PEC electrode at 0.70 V bias were achieved, respectively. The maximum hydrogen generation efficiency of 9.30% was obtained by using TiO$_2$ NBs as electrode, which was about 55% higher than that of using TiO$_2$ NWs as electrode. And the highest hydrogen generation efficiency of 13.15% was obtained by using TiO$_2$ NBs/Cu$_2$S composite structure as electrode, which was about 41% higher than that of TiO$_2$ NWs/Cu$_2$S composite structure, indicating the important role of TiO$_2$ hierarchical structure for water splitting.

The enhanced activity of the TiO$_2$ NBs/Cu$_2$S composite structure under UV irradiation can be interpreted using schematic diagrams as shown in Figs. 13 and 14. As we can see from Fig. 13, light would be reflected much more times among the branches of the TiO$_2$ NBs/Cu$_2$S composite structure than that of TiO$_2$ NWs/Cu$_2$S composite structure and the multiple reflections would extend the light propagation path, which is beneficial to the full utilization of incident light. The charge transfer processes and various energy gap
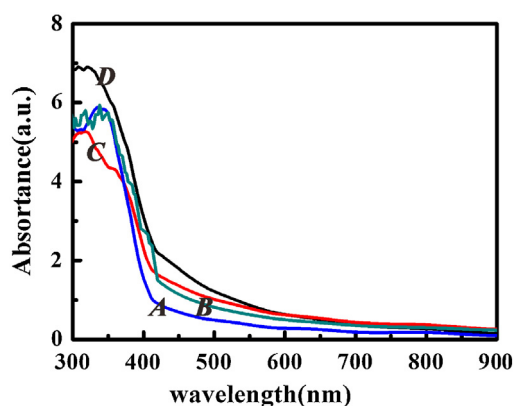

Fig. 11. UV–vis absorbance spectra of (A) TiO$_2$ NWs, (B) TiO$_2$ NBs, (C) TiO$_2$ NWs/Cu$_2$S composite structure of 10 cycles SILAR deposition, (D) TiO$_2$ NBs/Cu$_2$S composite structure of 10 cycles SILAR deposition.
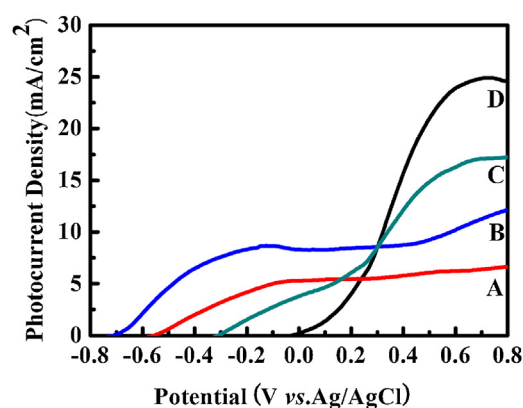

Fig. 12. Photocurrent density–voltage curves of as-prepared (A) TiO$_2$ NWs, (B) TiO$_2$ NBs, (C) TiO$_2$ NWs/Cu$_2$S composite structure of 10 cycles SILAR deposition, (D) TiO$_2$ NBs/Cu$_2$S composite structure of 10 cycles SILAR deposition.
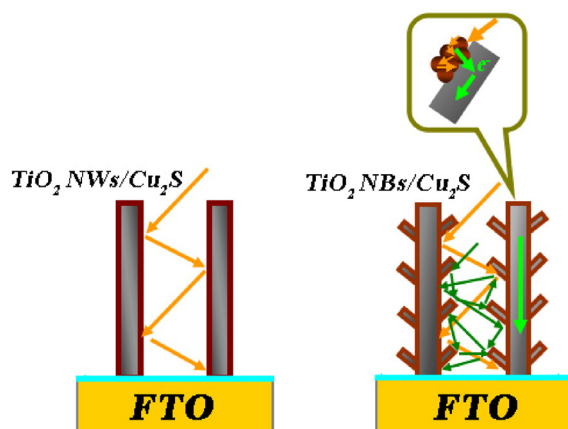
Fig. 13. Schematic representation of the utilization of incident sunlight.

structures of the samples obtained were exhibited in Fig. 14. The conduction band (CB) edge of Cu_2S (-4.44 eV vs absolute vacuum scale (AVS)) is higher compared with TiO_2 (-4.21 eV vs AVS); the valence band (VB) edges of Cu_2S and TiO_2 are located at -3.34 eV and -1.01 eV (vs AVS), respectively [37,38]. On the basis of the different positions of their band gaps, the photoexcited electrons can transfer from the conduction band of the Cu_2S shell to that of the TiO_2 core, contrarily, the photoexcited holes immigrate from the valence band of the TiO_2 core to that of the Cu_2S shell under UV irradiation. So the photo-induced electrons and holes have been effectively separated in the composite structure, which decreases the recombining ratio of photo-induced electrons and holes.

To investigate the influence of the thickness of Cu_2S film on the properties of as-obtained products, TiO_2 NBs/Cu_2S composite structure was synthesized with different SILAR cycles. Fig. 15 shows the characteristics of TiO_2 NBs/Cu_2S composite structure for photoelectrodes of different SILAR cycles. It can been seen that the photocurrent density of TiO_2 NBs/Cu_2S composite structure obtained with (A) 5 SILAR cycles, (B) 10 SILAR cycles,(C)15 SILAR cycles, was 11.20 mA cm^{-2} at 0.92 V versus Ag/AgCl, 24.85 mA cm^{-2} at 0.70 V versus Ag/AgCl, 16.94 mA cm^{-2} at 0.84 V versus Ag/AgCl, respectively. It was found obviously that TiO_2 NBs/Cu_2S composite
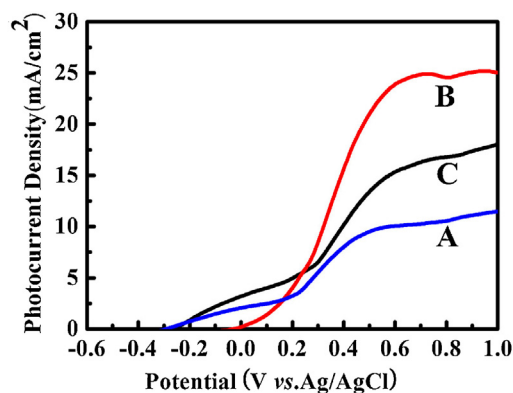

Fig. 15. Photocurrent density–voltage curves of TiO_2 NBs/Cu_2S composite structure obtained with varying SILAR cycles: (A) 5 cycles, (B) 10 cycles and (C) 15 cycles.
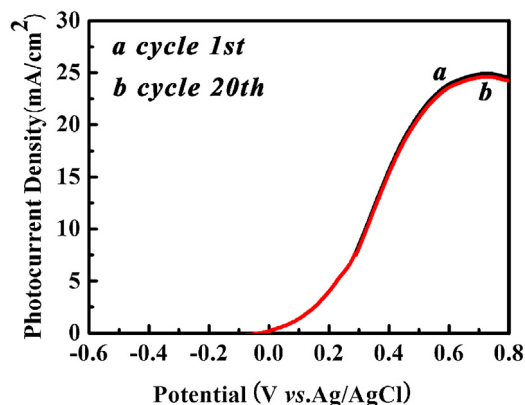

Fig. 16. Linear sweep voltammograms of the TiO_2 NBs/Cu_2S composite structure.

structure obtained with 10 SILAR cycles showed the highest photocurrent density, revealing a most suitable film thickness of Cu_2S film for photoelectrode.

Furthermore, to investigate the stability of as-obtained solar PEC electrodes, linear sweep voltammograms is measured after C–V scanning for 1 and 20 cycles under illumination, using TiO_2 NBs/Cu_2S composite structure obtained with 10 SILAR cycles as typical photoelectrodes, and the results were shown in Fig. 16. It is found obviously that the TiO_2 NBs/Cu_2S composite structure solar PEC electrode shows much more stable current density after C–V scanning under illumination for 20 cycles, revealing a better capability to resist photocorrosion.

4. Conclusion

In summary, TiO_2 NBs/Cu_2S composite structures were synthesized by SILAR on FTO conducting glass substrates for water splitting by using rutile TiO_2 nano-branched arrays as framework, which were prepared firstly using a simple two-step hydrothermal method. The synthetic process and working mechanism of the nanostructure were discussed. The optical property of composite structure was characterized, and enhanced absorption spectrum was discovered. Compared with the earlier studies, much higher hydrogen generation efficiency was obtained. Hydrogen generation efficiency of 13.15% at 0.70 V versus Ag/AgCl electrode was achieved with synthesized TiO_2 NBs/Cu_2S composite structure electrode due to the improved absorption and appropriate energy gap structure, which was over 40% higher than that of TiO_2 NWs/Cu_2S composite structure. The results demonstrate that the TiO_2 NBs/Cu_2S composite structure on FTO is desirable for PEC water splitting.
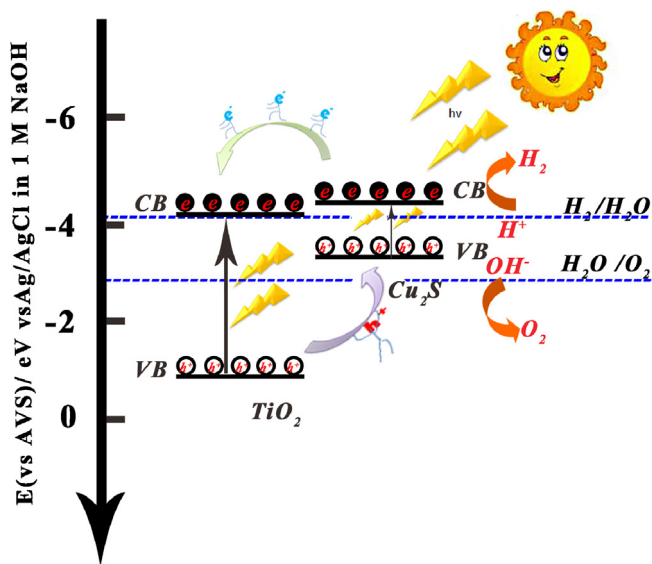

Fig. 14. Schematic representation of energy gap structures for TiO_2 NBs/Cu_2S composite structure.

Acknowledgement

References

[1] A. Fujishima, K. Honda, Nature 238 (1972) 37–38.
[2] L.X. Sang, Z.Y. Zhang, C.F. Ma, International Journal of Hydrogen Energy 36 (2011) 4732–4738.
[3] W.C. Chueh, C. Falter, M. Abbott, D. Scipio, P. Furler, S.M. Haile, A. Steinfeld, Science 330 (2010) 1797–1801.
[4] S.W. Boettcher, J.M. Spurgeon, C. Putnam, E.L. Warren, D.B. Turner-Evans, D. Kelzenberg, J.R. Maiolo, H.A. Atwater, N.S. Lewis, Science 327 (2010) 185–187.
[5] U.M. Shahed, A.S. Mofareh, W.B. Ingler, Science 297 (2002) 2243–2245.
[6] N.K. Allam, K. Shankar, C.A. Grimes, Journal of Materials Chemistry 18 (2008) 2341–2348.
[7] J.J. Goog, C.J. Lin, M.D. Ye, Y.K. Lai, Chemical Communications 47 (2011) 2598–2600.
[8] T. Kodama, N. Gokon, Chemical Reviews 107 (2007) 4048–4077.
[9] Y.S. Hu, A. Kleiman-Shwarsctein, A.J. Forman, D. Hazen, J.N. Park, E.W. McFarl, Journal of Materials Chemistry 20 (2008) 3803–3805.
[10] A. Wolcott, W.A. Smith, T.R. Kuyke, Y.P. Zhao, J.Z. Zhang, Advanced Functional Materials 19 (2009) 1849–1856.
[11] Y.B. Liu, H.B. Zhou, B.X. Zhou, J.H. Li, H.C. Chen, J.J. Wang, International Journal of Hydrogen Energy 36 (2011) 167–174.
[12] X.W. Wang, G. Liu, G.Q. Lu, H.M. Cheng, International Journal of Hydrogen Energy 35 (2010) 8199–8205.
[13] S.C. In, Z.B. Chen, J.F. Arnold, R.K. Dong, M.R. Pratap, F.J. Thomas, X.L. Zheng, Nano Letters 11 (2011) 4978–4984.
[14] V.K. Mahajan, S.K. Mohapatra, M. Misra, International Journal of Hydrogen Energy 33 (2008) 5369–5374.
[15] J.H. Park, S. Kim, A.J. Bard, Nano Letters 6 (2006) 24–28.
[16] Z.J. Jiang, Y.T. Tang, Q.L. Tay, Y.Y. Zhang, I.M. Oleksandr, D.P. Wang, J.Y. Deng, Y.K. Lai, H.F. Zhou, X.D. Chen, Z.L. Dong, Z. Chen, Advanced Energy Materials 3 (2013) 1368–1380.
[17] W.J. Zhou, X.Y. Liu, J.J. Cui, D. Liu, J. Li, H.D. Jiang, J.Y. Wang, H. Liu, CrystEngComm 13 (2011) 4557–4563.
[18] J.F. Xin, S. Karthik, O.K. Varghese, M. Paulose, J.L. Thomas, C.A. Grimes, Nano Letters 8 (2008) 3781–3786.
[19] B. Liu, E.S. Aydil, Journal of the American Chemical Society 131 (2009) 3985–3990.
[20] J.R. Jennings, A. Ghicov, L.M. Peter, P. Schmuki, A.B. Walker, Journal of the American Chemical Society 130 (2008) 13364–13372.
[21] J.Y. Kim, J.H. Noh, K. Zhu, A.F. Halverson, N.R. Neale, S. Park, K.S. Hong, A. Frank, ACS Nano 5 (2011) 2647–2656.
[22] H. Wang, Y.S. Bai, Q. Wu, W. Zhou, H. Zhang, J.H. Li, Journal of Chemical Physics 13 (2011) 7008–7013.
[23] Z.F. Liu, J.E.L. Ya, Y. Xin, W. Zhao, Materials Chemistry and Physics 120 (2010) 277–281.
[24] J.B. Veluru, K.K. Manippady, S.N. Appukuttan, L.K. Tan, I.A. Suleyman, R. Seeram, International Journal of Hydrogen Energy 37 (2012) 8897–8904.
[25] K.P. Sreenivasan, S.K. Harrison, C.M. Wu, P. Rui, J. Baltrusaitis, T.K. Ranjit, International Journal of Hydrogen Energy 37 (2012) 8257–8267.
[26] Y.J. Chi, H.G. Fu, L.H. Qi, K.Y. Shi, H.B. Zhang, H.T. Yu, Journal of Photochemistry and Photobiology A 195 (2008) 357–363.
[27] I. Robel, V. Subramanian, M. Kuno, V. Prashant Kamat, Journal of the American Chemical Society 128 (2006) 2385–2393.
[28] Z.J. Zhou, S.G. Yuan, J.Q. Fan, Z.L. Hou, W.H. Zhou, Z.L. Du, S.X. Wu, Nanoscale Research Letters 7 (2012) 652–660.
[29] Y.X. Li, Y.F. Hu, S.P. Peng, Journal of Physical Chemistry C 113 (2009) 9352–9358.
[30] S. Gorai, D. Ganguli, S. Chaudhuri, Materials Chemistry and Physics 88 (2004) 383–387.
[31] M. Savelli, T.J. Bouganot, Problems of the Cu_2S/CdS Cell, 31, Springer-Verlag, New York, 1979, pp. 213–256.
[32] M. Dachraoui, J. Vedel, Solar Cells 22 (1987) 187–194.
[33] I. Pintile, E. Pentia, L. Pintile, D. Petre, C. Constanstntin, T. Botila, Journal of Applied Physics 78 (1995) 1713–1718.
[34] E. Indrea, A. Barbu, Applied Surface Science 106 (1996) 498–501.
[35] I. Pop, C. Nascu, V. Ionescu, E. Indrea, I. Bratu, Thin Solid Films 307 (1997) 240–244.
[36] Z.Q. Sun, J.H. Kim, Y. Zhao, B.F. Bijar, V. Malgras, Y. Lee, Y.M. Kang, S.X. Dou, Journal of the American Chemical Society 133 (2011) 19314–19317.
[37] Y. Xu, M. Schoonen, American Mineralogist 85 (2000) 543–556.
[38] S.Q. Wei, Y.Y. Chen, Y.Y. Ma, Z.G. Shao, Journal of Molecular Catalysis A 331 (2010) 112–116.